2015

Structural health monitoring of localized internal corrosion in high temperature piping for oil industry

Thomas J. Eason
Iowa State University and BP Products North America

Leonard J. Bond
Iowa State University, bondlj@iastate.edu

Mark G. Lozev
BP Products North America

Structural health monitoring of localized internal corrosion in high temperature piping for oil industry

Abstract

Crude oil is becoming more corrosive with higher sulfur concentration, chloride concentration, and acidity. The increasing presence of naphthenic acids in oils with various environmental conditions at temperatures between 150°C and 400°C can lead to different internal degradation morphologies in refineries that are uniform, non-uniform, or localized pitting. Improved corrosion measurement technology is needed to better quantify the integrity risk associated with refining crude oils of higher acid concentration. This paper first reports a consolidated review of corrosion inspection technology to establish the foundation for structural health monitoring of localized internal corrosion in high temperature piping. An approach under investigation is to employ flexible ultrasonic thin-film piezoelectric transducer arrays fabricated by the sol-gel manufacturing process for monitoring localized internal corrosion at temperatures up to 400°C. A statistical analysis of sol-gel transducer measurement accuracy using various time of flight thickness calculation algorithms on a flat calibration block is demonstrated.

Keywords

Ultrasonics, Corrosion, Crude oil, Thin films, Chemical elements, Industry, Transducers, Solgels

Disciplines

Mechanics of Materials | Structures and Materials

Structural health monitoring of localized internal corrosion in high temperature piping for oil industry

Cite as: AIP Conference Proceedings **1650**, 863 (2015); https://doi.org/10.1063/1.4914690
Published Online: 02 April 2015

Thomas J. Eason, Leonard J. Bond, and Mark G. Lozev

Structural Health Monitoring of Localized Internal Corrosion in High Temperature Piping for Oil Industry

Thomas J. Eason[1,2 a)], Leonard J. Bond[1], and Mark G. Lozev[2]

[1]*Center for Nondestructive Evaluation, Iowa State University, Ames, IA 50011*
[2]*BP Products North America, Refining & Logistics Technology, Naperville, IL 60563*

[a)] easont@iastate.edu

Abstract. Crude oil is becoming more corrosive with higher sulfur concentration, chloride concentration, and acidity. The increasing presence of naphthenic acids in oils with various environmental conditions at temperatures between 150°C and 400°C can lead to different internal degradation morphologies in refineries that are uniform, non-uniform, or localized pitting. Improved corrosion measurement technology is needed to better quantify the integrity risk associated with refining crude oils of higher acid concentration. This paper first reports a consolidated review of corrosion inspection technology to establish the foundation for structural health monitoring of localized internal corrosion in high temperature piping. An approach under investigation is to employ flexible ultrasonic thin-film piezoelectric transducer arrays fabricated by the sol-gel manufacturing process for monitoring localized internal corrosion at temperatures up to 400°C. A statistical analysis of sol-gel transducer measurement accuracy using various time of flight thickness calculation algorithms on a flat calibration block is demonstrated.

INTRODUCTION

Oil refinery production of high quality clean fuels is becoming more challenging as a result of the changing world supply of crude oil towards properties of higher density, higher sulfur concentration, and higher acidity [1]. One such production challenge is an increased risk of corrosion from crudes with a high concentration of naphthenic acids [2]. The rate of naphthenic acid corrosion (NAC) is considered to be dependent on metallurgy, acid species, acid concentration, sulfur concentration, process temperature, shear stress, and the extent of a gas phase [3] resulting in a corrosion rate that is difficult to predict. The degradation morphology of NAC can be localized pitting at temperatures between 150°C and 400°C [4] resulting in challenging in-service inspection.

Varying acid concentration, flow rate, and temperature can result in three distinct damage mechanisms of uniform, non-uniform, and localized pitting [5]. Potential target application parameters for monitoring NAC are shown in Table 1.

TABLE 1. Potential target application parameters for NAC monitoring.

Parameter	Potential Target
Temperature	up to 400°C
Thickness Precision	0.05mm
Spatial Resolution Precision	0.05mm width & 0.05mm length
Pipe Wall Thickness	3-25mm
Pipe Diameter	>100mm
Metallurgy	Low-Alloy Steel (<9%Cr & <2.5% Mo)

41st Annual Review of Progress in Quantitative Nondestructive Evaluation
AIP Conf. Proc. 1650, 863-873 (2015); doi: 10.1063/1.4914690

NONDESTRUCTIVE EVALUATION REVIEW

Prior reviews of inspection and monitoring technologies for corrosion [6], upstream riser damage [7], water pipe condition [8], as well as general Non-Destructive Evaluation (NDE) sources [9, 10] are referenced for the following review of NDE methods for piping internal corrosion.

Optical

Endoscopy - Endoscopic techniques such as Close Circuit Television (CCTV) or boroscope inspection can capture internal pipe surface images as qualitative information. Quantitative 3D topography information and defect characterization can be obtained using various optical equipment configurations mounted on a crawler inside a pipe such as visual odometry [11] or laser ring triangulation [12].

Fiber Bragg Grating - Fiber Bragg gratings are manufactured by creating specific periodic variations of the refractive index of an optical fiber core. The refractive index interfaces in the fiber can be uniformly spaced such that reflected light at a particular wavelength, the Bragg wavelength, will undergo constructive interference in phase resulting in an amplified signal. An environmental change in temperature and strain of the fiber can be observed as the effective Bragg wavelength shift, λ_B/λ, in Eq. 1 with λ_B as the Bragg wavelength, α as the thermal expansion, ξ as the thermo-optic coefficient, ΔT as the change in temperature, ρ_e as the photo-elastic constant of the fiber core material, and ε as the longitudinal strain [13]. Monitoring strain in a structure can provide an early indicator for fatigue failure, but strain measurements are proposed to detect an increase in hoop (circumferential) stress as the result of wall thinning due to corrosion in a pipeline [14] as shown in Eq. 2 with t as the average wall thickness, r as the average pipe radius, P as the relative internal pressure, σ as the hoop stress, and E as Young's modulus.

$$\frac{\lambda_B}{\lambda} = (\alpha + \xi)\Delta T + (1 - \rho_e)\varepsilon \tag{1}$$

$$t = \frac{rP}{\sigma} = \frac{rP}{\varepsilon E} \tag{2}$$

Electromagnetic

Electromagnetic inspection involves the generation, interaction, and measurement of electromagnetic fields to detect the relative material conductivity and permeability of a test component.

Conventional Eddy Current - A periodic magnetizing coil perpendicular to a conductive surface will create a primary magnetic flux, Φ_p, described in Eq. 3 with N_p as the primary number of coils, I_p as the primary excitation current, ω as angular frequency, and t as time. The oscillating primary magnetic flux induces circulatory eddy currents which in turn create a secondary magnetic flux, Φ_s, in opposition to the primary magnetic flux. The equilibrium flux, Φ_e, described in Eq. 4, is measured by a change in coil impedance as a result of a change in the surface material conductivity or permeability. The penetration depth in mm, d, is described in Eq. 5, with ρ as electrical resistivity in Ω-cm, f as excitation frequency, and μ_r as a dimensionless relative permeability.

$$\Phi_p \propto N_p I_p \sin(\omega t) \tag{3}$$

$$\Phi_e = \Phi_p - \Phi_s \tag{4}$$

$$d = 50\sqrt{\rho / f\mu_r} \tag{5}$$

Remote Field Eddy Current - The measurement of phase lag from an exciter coil to a pickup coil placed inside a pipe has a linear relationship to wall thickness. The phase lag, θ, is described in Eq. 6 with x as distance between coils, f as excitation frequency, μ as average permeability, and σ as electrical conductivity between the two coils.

$$\theta = x\sqrt{\pi f \mu \sigma} \tag{6}$$

Pulsed Eddy Current - In pulsed eddy current, a step function voltage is applied and emits electromagnetic pulses onto the outer pipe surface. The decaying magnetic field induces eddy currents that diffuse through the wall and then rapidly decay at the pipe inside surface. The voltage induced by the eddy currents can be measured in the time domain and correlated to wall thickness based on the point in time at which rapid signal decay occurs.

Radiographic

Radiographic inspection involves the transmission, propagation, attenuation, measurement, and interpretation of energy from a source, through an object, and onto a film or detection device.

Energy Source - The most typical energy source is electromagnetic photon radiation such as Gamma rays that emit from unstable isotopes, or X-rays that are released from an unstable condition as high speed electrons strike a target. Sub-atomic particle energy sources such as thermal neutrons or protons can be used with limited application.

Attenuation - Generated gamma ray intensity is directly related to the number of atoms present in the isotope source material. Generated X-ray intensity is a function of wavelength and tube voltage. The intensity of a beam of radiation exiting a material, I, is shown as Eq. 7 with I_0 as the radiation beam intensity entering a material, μ as the linear attenuation coefficient, and x as material thickness. The linear attenuation coefficient is further described in Eq. 8 with N as Avogradro's constant, σ as the total atomic attenuation coefficient, ρ as the material density, and A as the atomic mass. The total atomic attenuation coefficient is further described in Eq. 9 with σ_{pe} as the photoelectric effect, σ_s as Compton scattering and coherent (or Rayleigh) scattering, σ_{pp} as pair production, and σ_{pd} as photodisintegration.

$$I = I_0 e^{-\mu x} \tag{7}$$

$$\mu = \frac{N\sigma\rho}{A} \tag{8}$$

$$\sigma = \sigma_{pe} + \sigma_s + \sigma_{pp} + \sigma_{pd} \tag{9}$$

Detectors - Individual grains of traditional radiographic film react and darken with radiation exposure as shown in Eq. 10 with E as the film exposure, I_f as the radiation intensity on the film, and T as the time of exposure. When viewing film, interpretations are made based on the observed contrast described in Eq. 11 with D as the density observed on the film, and G_D as the contrast measured at density D. Observed film density is further defined in Eq. 12 with I_0 as the intensity of the viewing light source, and I_t as the intensity observed on the film.

$$E = I_f T \tag{10}$$

$$G_D = \frac{dD}{d\left(\log E\right)} \tag{11}$$

$$D = \log \frac{I_0}{I_t} \tag{12}$$

Computed Radiography - Computed Radiography refers to flexible imaging plates similar to traditional film, but rather the plates are exposed, digitally scanned, and the reused via a photo-stimulable phospors storage process.

Digital Radiography - Digital Radiography (can also be described as Real-Time Radiography) refers to flat panel detectors composed of amorphous silicon (or other scintillating material) arrays, and thin film transistors to display an image at the same time that radiation is passing through the object.

Orientation - The common configuration is to have both source and detector external to the pipe of interest. An orthogonal external orientation places the source perpendicular to the top surface and the detector perpendicular to the bottom surface of the pipe. A tangential external orientation places the source tangential to the pipe as to focus the beam only through an edge chord section of the pipe wall with the detector placed in a tangential receiving orientation, often used in applications with higher material density. A backscatter orientation places the source and detector outside the pipe at an angle best suited to receive Compton scattered photons. An alternative configuration can have the source placed inside the pipe with multiple curved detectors circumferentially outside the pipe.

Computed Tomography - The source and detector are rotated relative to the object to collect multiple cross-section images which are then reconstructed to generate a composite image of relatively high accuracy.

Acoustic

Acoustic Emission - A pipe deformed under stress will generate elastic waves referred to as acoustic emissions (AE). The source of such pipe stress is mechanical or thermal loading from normal operations; although, additional loading can be applied for short duration AE inspections. During AE monitoring, a baseline environmental noise measurement is collected and subsequent measurements are compared to the baseline. Low amplitude changes from

the baseline can be attributed to plastic deformations, microstructural changes, chemical reactions related to corrosion, or flaking or removal of corrosion products from a surface. High amplitude changes from the baseline can be generated by the growth of flaw-like cracks that introduce stress in the lattice.

Ultrasonic

Ultrasonic NDE inspection of steel components consists of the transmission and measured reception of acoustic energy using a wide range of possible system configurations. It is possible to organize the different configurations into the following five categories: wave mode, wave coverage, transduction method, transducer motion, and transducer configuration. Listed are some of the potential types of wave modes: bulk longitudinal, bulk shear horizontal, bulk shear vertical, surface longitudinal creeping, surface Rayleigh, guided transverse, guided symmetric lamb, and guided asymmetric lamb; potential types of wave coverage: single point, point array, sparse array, tomographic array, mid-range, and long-range; potential types of transduction methods: piezoelectric, electromagnetic acoustic transduction (EMAT), magnetostrictive, and laser; potential types of transducer motion: manual, semi-automated, fully-automated, and permanent installation; and potential types of transducer configurations: pulse-echo, pitch-catch, and various simultaneous interactions between multiple transducers in an array such as phased array electronic scanning, beam steering, and beam focusing.

Bulk Wave Thickness Measurement - An ultrasonic transducer acoustically coupled to the outside of a pipe can be excited with a voltage pulse to transmit a bulk wave from the transducer, through the pipe outside surface interface, through the pipe wall, reflected back from the pipe inside surface interface, back through the pipe wall, back through the pipe outside surface interface, and finally received by the same or another transducer. A simplified one-dimensional wave equation for elastic bulk wave propagation is shown in Eq. 13 with ρ as mass density, u as the wave front particle displacement, t as time, C as the speed of sound, and x as distance. The speed of sound for longitudinal, C_l, and transverse, C_t, waves are shown in Eq. 14 & 15 with λ and μ as Lamé's first and second parameters, E as Young's modulus, ν as Poisson's ratio, and G as the shear modulus. The temperature influence on the elastic moduli has been found to be approximately linear as shown in Eq. 16, with $C°$ as the wave speed at a reference temperature, dC/dT as a speed change constant, and ΔT as the temperature change.

$$\rho \frac{\partial^2 u}{\partial t^2} = C^2 \frac{\partial^2 u}{\partial x^2} \tag{13}$$

$$C_l = \sqrt{\frac{\lambda + 2\mu}{\rho}} = \sqrt{\frac{E(1-\nu)}{(1+\nu)(1-2\nu)\rho}} \tag{14}$$

$$C_t = \sqrt{\frac{\mu}{\rho}} = \sqrt{\frac{G}{\rho}} = \sqrt{\frac{E}{2(1+\nu)\rho}} \tag{15}$$

$$C = C° - (dC/dT)\Delta T \tag{16}$$

The time domain harmonic motion solution to Eq. 13 is shown as Eq. 17 with A as the maximum particle displacement amplitude, ω as the angular frequency, and k as the angular wave number. The relation between wavelength, λ, frequency, f, wave speed, C, and wave number, k, are shown as Eq. 18-20.

$$u = Ae^{i(kx-\omega t)} \tag{17}$$

$$f = \omega/(2\pi) \tag{18}$$

$$\lambda = C/f = (2\pi C)/\omega \tag{19}$$

$$k = \omega/C \tag{20}$$

As a sound wave reaches an interface between two different materials, the proportion reflected depend on the acoustic impedance mismatch between the two materials as shown in Eq. 21 & 22 with R as the reflection coefficient, z_1 as the incident material acoustic impedance and z_2 as the transmission material acoustic impedance. Given z_1 as a metal and z_2 as a fluid, $z_1 >> z_2$ resulting in a strong reflected signal as R = -1 as is the case of a back-wall reflection from an inside pipe wall surface.

$$z = \rho C \tag{21}$$

$$R = \frac{z_2 - z_1}{z_2 + z_1} \tag{22}$$

The thickness of the pipe wall, d, can be computed from Eq. 23 with C as the speed of sound in the material, and t_r as the total round trip time between transducer excitation and reception.

$$d = \frac{Ct_r}{2} \tag{23}$$

The received voltage signal can be processed using various filtering and envelope wrapping techniques and analyzed using various time-of-flight calculation algorithms; these various calculation methods will result in different thickness measurement values [15, 16]. The manual bulk wave technique requires the temporary coupling of an ultrasonic sensor to a pipe exterior. Permanently installed piezoelectric ultrasonic bulk wave sensors of various wave mode, frequency, footprint, and coupling designs are possible above ambient temperatures [17, 18, 19].

Guided Waves - Long range guided waves in a piping system are generated by a circumferential transducer; the waves propagate between the inside surface boundary and outside surface boundary of the pipe in torsional, longitudinal, or transverse wave modes. The propagating wave can become distorted and have a partial mode conversion when encountering a cross-sectional area change in the pipe wall such as a weld or a region of localized corrosion. In a pulse-echo configuration, lower energy waves are reflected back to the transducer to be received and interpreted. The magnitude of the cross-sectional change associated with a reflection is relative to the received signal amplitude; the longitudinal location of the cross-sectional change can be determined by the signal arrival time; the circumferential location of the cross-sectional change can be determined only when using a circumferential array transducer by measuring the relative signal amplitude received by each element in the array. The same principles apply to higher frequency medium range guided wave techniques which generate and propagate waves in a pipe longitudinal and circumferential direction using various types of array configurations over distances generally less than 3 meters. In medium range guided wave, cross-sectional area changes from reflected signals in the sound path can be measured in a pulse-echo configuration, attenuation can be measured using a pitch-catch configuration, and average wall thickness of the sound path can be correlated from the appropriate dispersion curve to a change in acoustic velocity measured by a change in signal arrival time in a pitch-catch configuration. A tomographic inversion technique can also be applied in certain medium range guided wave configurations.

Transduction - Different transduction methods can generate and receive elastic waves of different mode, frequency, and amplitude combinations by using various conversion processes between electrical energy and mechanical/vibration/elastic energy. Piezoelectric transducers exhibit the piezoelectric effect as a reversible interaction between electrical charge and mechanical stress on a crystalline or ceramic material and are the most common transduction method for industrial applications. Magnetostrictive transducers utilize magnetostriction as a reversible interaction between an applied electromagnetic field and a dimensional change from domain shifting and rotation in a ferromagnetic material. Electromagnetic Acoustic Transducers (EMAT) induce eddy currents in the surface region which then interact with a permanent magnetic field and generate elastic ultrasonic waves directly in the component via the Lorentz mechanism in conductive materials and by magnetostriction in ferromagnetic materials; both as reversible processes. Laser transduction involves a generation laser and a detection laser. The generation laser quickly heats a small area on the surface causing sudden thermal expansion and the associated stress reactions can generate elastic waves; the detection laser can measure dimensional changes on the surface from elastic waves via interferometry. A low acoustical impedance interface is necessary between piezoelectric and magnetostrictive transducers and the pipe surface to directly transfer mechanical stresses; rather, this coupling is not necessary for EMAT and laser transduction methods.

Element Arrays - The acoustic characteristics of an ultrasonic element phased array probe can be modified electronically by introducing time shifts in signals sent to and received from individual elements. The dynamic control of the beam properties and dynamic focusing can lead to improved measurement precision for various wave modes. Beam manipulations include: electronic scanning achieved by pulsing a group of elements along a transducer in sequence, beam steering achieved by delaying the pulsing of each element at a set rate, and beam focusing achieved by varying the rate of delay of the pulsing of each element. A tomographic technique can also be applied using element arrays to collect multiple cross-section signals which are then reconstructed and processed to generate a composite image. Finally, another technique that can be applied is Full Matrix Capture involving the sequential excitation of individual elements and reception by all elements in the array followed by the reconstruction of the image using the Total Focusing Method (TFM) to time-shift each received signal according to the focal laws for each element.

THICKNESS MONITORING ACCURACY EXPERIMENT

An experiment was conducted to demonstrate a statistical modeling approach to compare measurement accuracy of multiple bulk wave ultrasonic thickness calculation algorithms: a local maxima method (Peak-to-Peak), a threshold method (Zero Crossing), and an optimum correlation method (Cross Correlation) [15] were investigated.

Experiment Setup

A total of forty four sol-gel sensor elements were directly deposited [19, 20] in 2x2 array groups onto a flat step calibration block with a 0.10 mm step size from 3.00 mm to 4.00 mm as shown in Fig. 1. The elements have an average center frequency of 13.1 MHz and an average bandwidth of 8.2 MHz at -6dB as shown in Fig. 2 using a 100 MHz sampling frequency. The gain for each element was individually set for the first back-wall reflection. A total of thirty seven pulse-echo waveforms were collected for each of the sensor elements over a period of ninety minutes as shown in Fig. 3. The first and second signal gates were established to be identical in terms of height, location, and width for all 1628 waveforms. A negative amplitude gate height was used due to the signal asymmetry.

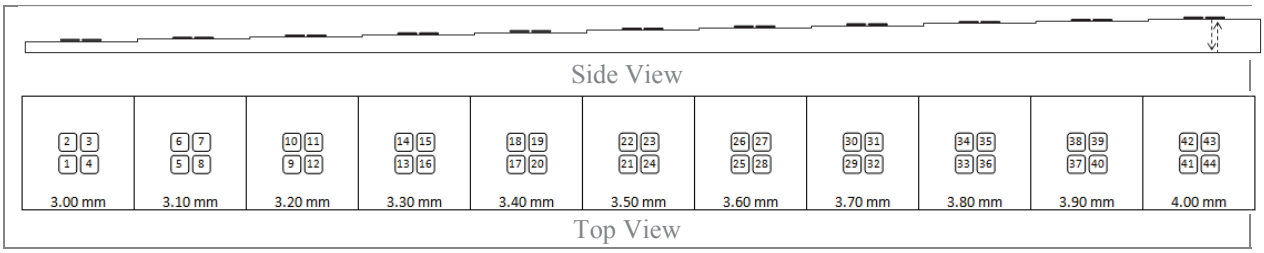

FIGURE 1. Schematic of 3-4 mm calibration block with deposited sol-gel sensor elements.

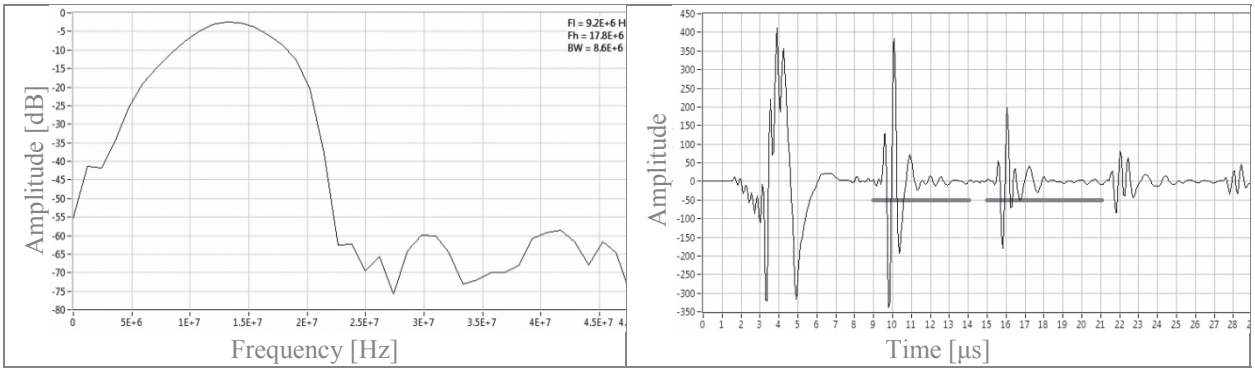

(a) (b)

FIGURE 2. a) Typical frequency domain plot. b) Typical pulse-echo signal response with gates.

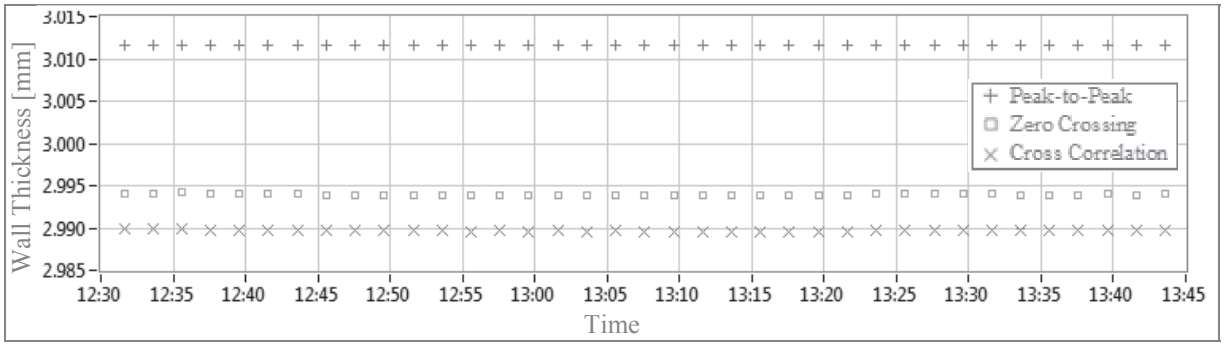

FIGURE 3. Single element thickness measurements over time for various time-of-flight algorithms.

The thirty seven thickness measurements over time were averaged for each sensor element for each of the three algorithms for a range of acoustic velocity values between 5870 and 5930 m/s. These time average thickness measurements were subtracted from the step calibration block true thickness to produce residual thickness values for each velocity value for each algorithm and for each element. These residual thickness values for the forty four elements were averaged, with outliers excluded, and shown in Table 2. The absolute residual thickness was minimized using a least squared regression to find the ideal velocity for each algorithm. The following analysis used the average of the three ideal velocities at 5905 m/s.

TABLE 2. Average residual thickness values for velocities and algorithms.

Velocity	Peak-to-Peak	Zero Crossing	Cross Correlation
5870 m/s	-0.0241 mm	-0.0240 mm	-0.0143 mm
5880 m/s	-0.0181 mm	-0.0179 mm	-0.0084 mm
5890 m/s	-0.0122 mm	-0.0120 mm	-0.0024 mm
5900 m/s	-0.0062 mm	-0.0060 mm	0.0035 mm
5910 m/s	-0.0003 mm	-0.0002 mm	0.0095 mm
5920 m/s	0.0056 mm	0.0058 mm	0.0154 mm
5930 m/s	0.0116 mm	0.0117 mm	0.0213 mm
Ideal Velocity	5910 m/s	5910 m/s	5894 m/s

Experiment Analysis

The measured thickness values are compared to the calibration block thickness values in Fig. 4 showing eight Peak-to-Peak outliers and one Cross Correlation outlier. All eight Peak-to-Peak outliers coincide with a local second peak with greater absolute amplitude compared to the local first peak as shown in Fig. 5a; the larger second peak is mistakenly identified resulting in an outlier thickness measurement. These outliers could be avoided by analyzing the rectified signal, algorithm modification, or gate adjustment; although these steps were not taken at this time.

The residual thickness values are plotted relative to the calibration block thickness in Fig. 5b showing that the residual variation appears to be random relative to calibration block thickness. The distribution of residual values and absolute residual values can be observed in Fig. 6.

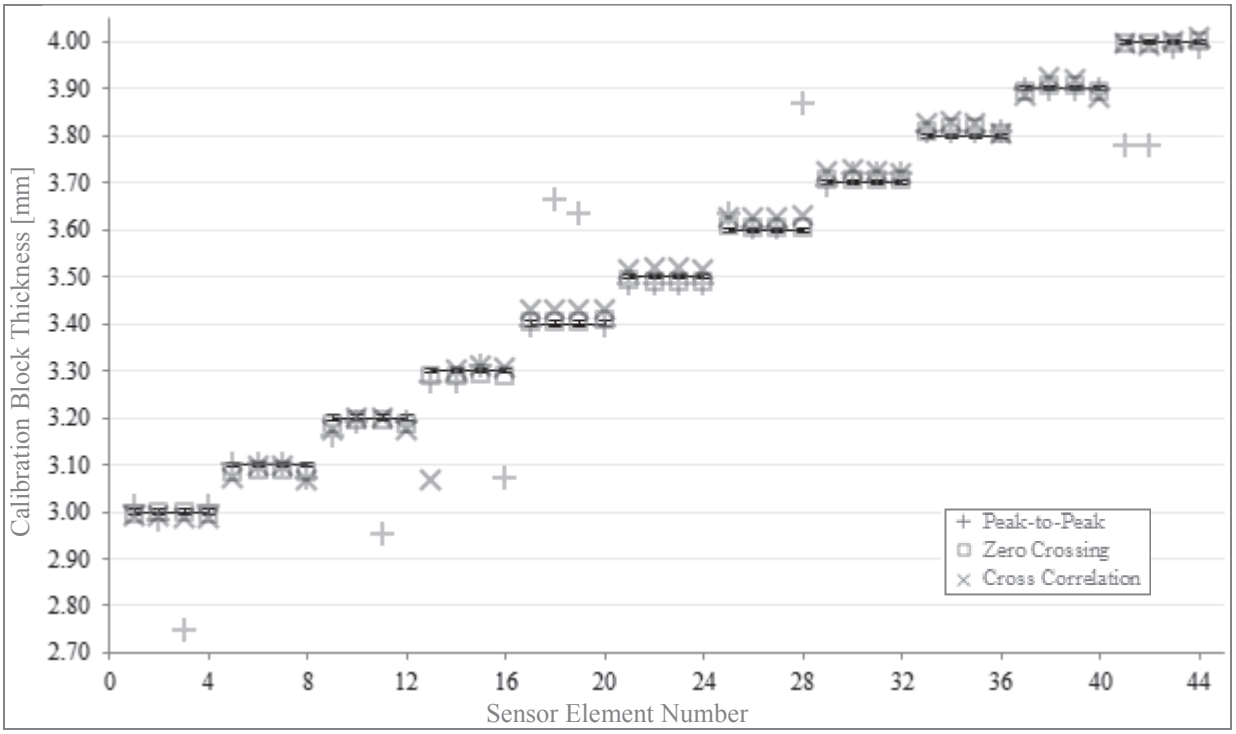

FIGURE 4. Measured thickness compared to calibration block thickness for each sensor element.

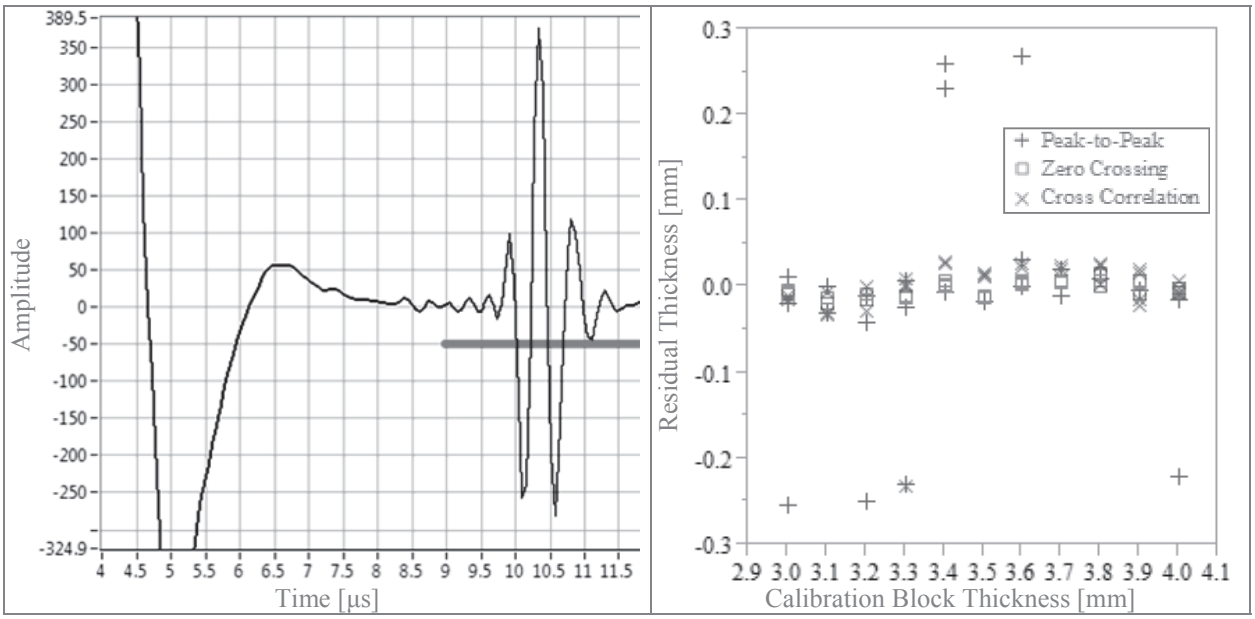

(a) (b)

FIGURE 5. a) Peak-to-Peak outlier caused by a second local peak with greater absolute amplitude. b) Residual thickness variation and outliers appear to be random as compared to calibration block thickness.

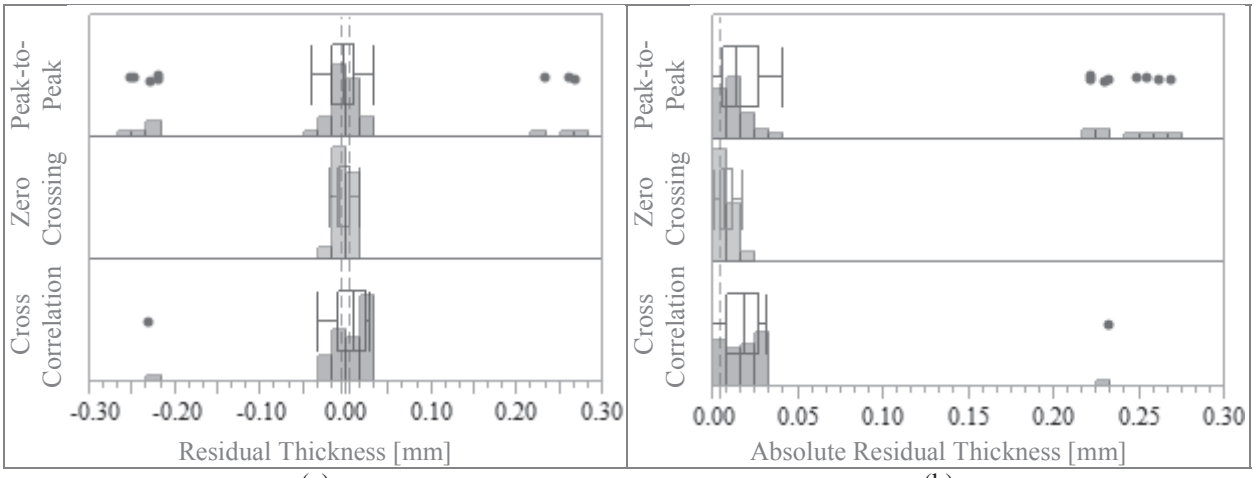

(a) (b)

FIGURE 6. Box plots and histograms for a) Residual Thickness and b) Absolute Residual Thickness. The vertical dashed lines indicate the 0.005mm calibration block machining accuracy.

The absolute residual values could be analogous to flaw size in a Probability of Detection (POD) analysis described in MH-1823 [21] where distribution models quantify measurement performance. A loglogistic cumulative distribution is described in Eq. 24 [22] with t as the absolute residual thickness, μ as the mean, and σ as the standard deviation. This model provided an adequate fit to the absolute residual values for all three algorithms as shown in Fig. 7 with data left censored data at 0.005 mm due to machining accuracy. The measurement accuracy is quantified in Tables 3 & 4 with and without outlier data points; these values are ideal considering precise velocity calibration, smooth uniform back-wall reflective surface, minimal temperature fluctuations, and no system degradation.

$$F(t;\mu,\sigma) = \Phi_{\log is}\left(\frac{\log(t)-\mu}{\sigma}\right) \qquad \Phi_{\log is}(z) = \exp(z)/[1+\exp(z)] \tag{24}$$

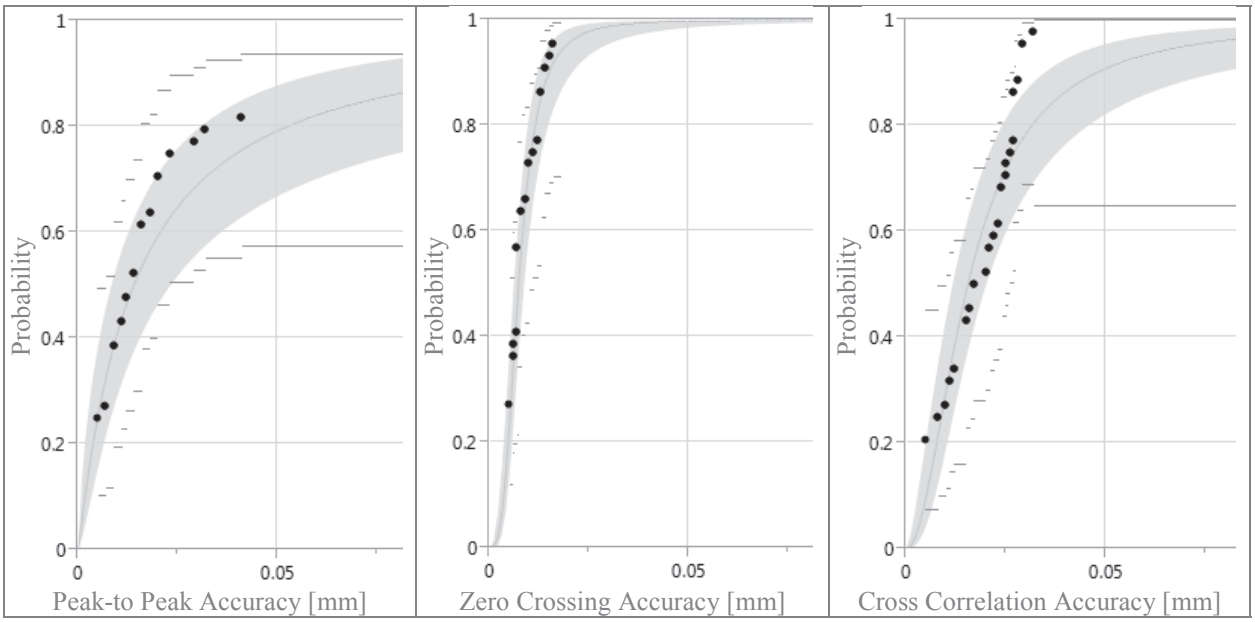

FIGURE 7. Cumulative distribution of absolute residual values (points) with 95% nonparametric confidence intervals (horizontal bars) and parametric loglogistic model (curve) with 95% confidence interval (shaded region) for a) Peak-to-Peak b) Zero Crossing and c) Cross Correlation. Outlier points are outside coordinate range and not visible in figure. Results are preliminary.

TABLE 3. Probability of a measurement to be within 0.05mm of actual calibration block thickness.

Model	Accuracy	Peak-to-Peak	Zero Crossing	Cross Correlation	Peak-to-Peak No Outliers	Cross Correlation No Outliers
Nonparametric	Estimate	81.8%	100%	97.7%	100%	100%
	Lower 95% Interval	67.7%	100%	65.3%	100%	100%
Loglogistic	Estimate	79.3%	99.7%	90.8%	95.9%	92.7%
	Lower 95% Interval	67.0%	98.5%	82.3%	88.6%	85.0%

TABLE 4. Expected measurement accuracy for equivalent a_{90} and $a_{90/95}$ values.

Model	Probability	Peak-to-Peak	Zero Crossing	Cross Correlation	Peak-to-Peak No Outliers	Cross Correlation No Outliers
Loglogistic	90% Accuracy [a_{90}]	0.11mm	0.02mm	0.05mm	0.03mm	0.04mm
	Lower 95% Interval of 90% Accuracy [$a_{90/95}$]	0.32mm	0.02mm	0.08mm	0.03mm	0.07mm

CONCLUSIONS

Motivated by the increase of naphthenic acids in crude oils, a review of inspection and monitoring technologies for piping internal corrosion was provided. In addition, a statistical modeling method for Structural Health Monitoring (SHM) measurement accuracy in an ideal environment using a small sample of sol-gel compression wave sensors was demonstrated for three time-of-flight thickness calculation algorithms. The reported accuracy values for each algorithm are preliminary. More robust statistical methods can be applied to additional real and simulated measurements under various system and environmental conditions in order to draw a true conclusion.

ACKNOWLEDGMENTS

This work supported by BP Products North America and Applus RTD Technological Center in the Netherlands.

REFERENCES

1. W. Qing, "Processing high TAN crude: part I," *Petroleum Technology Quarterly,* pp. 35-43, Q4 2010.
2. F. Ropital, "Current and future corrosion challenges for a reliable and sustainable development of the chemical, refinery, and petrochemical industries," *Materials and Corrosion,* vol. 60, no. 7, pp. 495-500, 2009.
3. E. Slavcheva, B. Shone and A. Turnbull, "Review of naphthenic acid corrosion in oil refining," *British Corrosion Journal,* vol. 34, no. 2, pp. 125-131, 1999.
4. American Petroleum Institute, "Damage Mechanisms Affecting Fixed Equipment in the Refining Industry," API Publishing Services, Washington, 2011.
5. X. Q. Wu, H. M. Jing, Y. G. Zheng, Z. M. Yao and W. Ke, "Study on high-temperature naphthenic acid corrosion and erosion-corrosion of aluminized carbon steel," *Journal of Materials Science,* vol. 39, no. 3, pp. 975-985, 2004.
6. R. E. Beissner and A. S. Birring, "Nondestructive Evaluation Methods for Characterization of Corrosion: State of the Art Review," Nondestructive Testing Information Analysis Center, San Antonio, Texas, 1988.
7. M. G. Lozev, R. W. Smith and B. B. Grimmett, "Evaluation of methods for detecting and monitoring of corrosion damage in risers," *Journal of Pressure Vessel Technology - Transactions of the ASME,* vol. 127, no. 3, pp. 244-254, 2005.
8. Z. Liu and Y. Kleiner, "State of the art review of inspection technologies for condition assessment of water pipes," *Measurement,* vol. 46, no. 1, pp. 1-15, 2013.
9. D. E. Bray and R. K. Stanley, Nondestructive Evaluation: A Tool in Design, Manufacturing, and Service, Boca Raton: CRC Press - Taylor & Francis Group, 1997.
10. ESR Technology Ltd., "The HOIS Interactive Knowledge Base," [Online]. Available: http://hois-ikb.esrtechnology.com/. [Accessed July 2014].
11. P. Hansen, H. Alismail, P. Rander and B. Browning, "Pipe Mapping with Monocular Fisheye Imagery," in *IEEE/RSJ International Conference on Intelligent Robots and Systems (IROS)*, Tokyo, 2013.
12. O. Duran, K. Althoefer and L. D. Senevatne, "Automated pipe defect detection and categorization using camera/laser-based profiler and artificial neural network," *IEEE Transactions on Automation Science and Engineering,* vol. 4, no. 1, pp. 118-126, 2007.
13. M. Majumder, T. K. Gangopadhyay, A. K. Chakraborty, K. Dasgupta and D. K. Bhattacharya, "Fibre Bragg gratings in structural health monitoring - Present status and applications," *Sensors and Actuators A-Physical,* vol. 147, no. 1, pp. 150-164, 2008.
14. R. C. Tennyson, N. Banthia, E. Rivera, S. Huffman and I. Sturrock, "Monitoring structures using long gauge length fibre optic sensors," *Canadian Journal of Civil Engineering,* vol. 34, no. 3, pp. 422-429, 2007.
15. B. Barshan, "Fast processing techniques for accurate ultrasonic range measurements," *Measurement Science & Technology,* vol. 11, no. 1, pp. 45-50, 2000.
16. A. J. C. Jarvis and F. B. Cegla, "Application of the distributed point source method to rough surface scattering and ultrasonic wall thickness measurement," *Journal of the Acoustical Society of America,* vol. 132, no. 3, pp. 1325-1335, 2012.
17. GE Sensing & Inspection Technologies, "GE Measurement & Control - Rightrax High Temperature (HT)," December 2009. [Online]. Available: http://www.ge-mcs.com/download/ultrasound/corrosion-monitoring/GEIT-20212EN_rightrax-ht-specifications.pdf. [Accessed April 2014].
18. F. B. Cegla, P. Cawley, J. Allin and J. Davies, "High-Temperature (>500 degrees C) Wall Thickness Monitoring Using Dry-Coupled Ultrasonic Waveguide Transducers," *IEEE Transactions on Ultrasonic Ferroelectrics and Frequency Control,* vol. 58, no. 1, pp. 156-167, 2011.
19. M. Kobayashi, C. -K. Jen, J. F. Bussiere and K. -T. Wu, "High-temperature integrated and flexible ultrasonic transducers for nondestructive testing," *NDT & E International,* vol. 42, no. 2, pp. 157-161, 2009.
20. D. A. Barrow, T. E. Petroff and M. Sayer, "Method for producing thick ceramic films by a sol gel coating process". United States of America Patent 5,585,136, 17 December 1996.
21. "MIL-HDBK-1823A - Nondestructive Evaluation System Reliability Assessment," Department of Defense - United States of America, Dayton, 2009.

22. W. Q. Meeker and L. A. Escobar, Statistical Methods for Reliability Data, New York: John Wiley & Sons, Inc., 1998.